Mechanical Systems and Signal Processing 225 (2025) 112268

Contents lists available at ScienceDirect

Mechanical Systems and Signal Processing

journal homepage: www.elsevier.com/locate/ymssp

Full Length Article

Catapult mechanism-enabled push-button energy harvester designed for capturing ultra-low frequency motion

Yihao Li [1], Xuzhang Peng [1], Yizhou Li, Dian Li, Guobiao Hu [*]

Thrust of Internet of Things, The Hong Kong University of Science and Technology (Guangzhou), Nansha, Guangzhou 511400, China

ARTICLE INFO

Keywords:
Catapult mechanism
Ultra-low frequency
Electromagnetic energy harvesting
Energy management

ABSTRACT

The dominant ultra-low frequencies of ambient vibrations pose a significant challenge for highly efficient energy harvesting. To address this challenge, this study introduces a catapult mechanism-enabled push-button energy harvester (CMPEH) designed to capture ultra-low frequency motion. It primarily comprises a motion converter, a unique catapult mechanism, and an electromagnetic transducer. Their synergistic operation transforms small, ultra-low frequency push-button actions into swift, amplified kinetic motion, allowing the proposed CMPEH to generate a large output. A simplified theoretical model was developed to provide insights into the working principle of the CMPEH and guide its design. Simulations and experiments were conducted to assess the performance. It was noted that the buffer springs play crucial roles in affecting the output. An investigation showed that within the tested spring stiffness range (0.29–0.98 N/mm), the RMS power output of the harvester increased significantly as the spring stiffness increased meanwhile, the duration for the magnet to traverse the coils reduced from 0.113 s to 0.053 s. With an external load of 290 Ω, the harvester could produce a maximum peak-to-peak voltage of 40.54 V and achieve a power density of 241.92 W/m^3 at a spring stiffness of 0.98 N/mm. Moreover, application demonstrations were conducted, showing that subjected to a single excitation, the CMPEH could light up around 4500 LED bulbs (rated voltage 1.60 V) and drive a humidity and temperature sensor to function for about 30 s. In general, the results indicated that the proposed CMPEH excels in capturing ultra-low frequency ambient vibrations below 1 Hz and converting them into electricity. The approaches and findings presented in this study offer guidelines for the development of future self-powered systems by utilizing ultra-low frequency vibration energy.

1. Introduction

With the rapid development of the Internet of Things (IoT), many innovative concepts have emerged, such as smart cities, buildings, and industries. In this context, an increasing number of IoT node devices are being used for various monitoring applications [1–6]. However, most IoT node devices rely on municipal power grids or chemical batteries for power supply sources [7]. From a long-term perspective, existing power supply solutions not only restrict the widespread utilization of IoT node devices but also lead to substantial maintenance costs, e.g., battery replacement or recharging. One promising solution to address the above issues is the

* Corresponding author.
E-mail address: guobiaohu@hkust-gz.edu.cn (G. Hu).
[1] These authors contribute equally to this paper.

https://doi.org/10.1016/j.ymssp.2024.112268
Received 13 August 2024; Received in revised form 15 December 2024; Accepted 21 December 2024
Available online 6 January 2025

vibration energy harvesting technology.

Vibration energy harvesters (VEHs) can convert ambient mechanical energy, typically characterized by ultra-low frequencies [8], from human motions [9], railway systems [10], and natural phenomena such as wind [11,12], tides [13] into electricity via electrostatic [14], electromagnetic [15–18], piezoelectric [19–23], and triboelectric [24–28] transduction mechanisms. A well-designed vibration energy harvester can capture significant energy from its surrounding environment. For instance, Qi *et al.* [10] conducted a review of energy harvesting technologies utilized in railway systems, and their findings suggest that vibration energy harvesting holds great promise. Priya *et al.* [29] designed a piezoelectric windmill with 12 bimorphs arranged around a rotating shaft. The harvester they prototyped could generate a power of 10.20 mW at the excitation frequency of 6 Hz. Minami *et al.* [30] developed a hybrid energy harvester using an unimorph piezoelectric energy harvester (PEH) and permanent magnets. In the field test, the device could harvest energy from human motion and generate a maximum power of 1.2 μW at an optimal resistance of 600 kΩ. Asadi *et al.* [31] designed a novel pavement to harvest energy from human footsteps. The pavement harvester generates a power output of 0.57 W when a person walks on it, with each step producing 511.00 mJ with a 900 cm^2 tile. Hou *et al.* [32] proposed a rotational pendulum hybrid generator that integrates triboelectric and electromagnetic mechanisms. At a driving frequency of 2 Hz and an excitation amplitude of 14 cm, the maximum power densities produced by the triboelectric nanogenerator (TENG) and the electromagnetic generator (EMG) were 79.90 and 3.25 W/m^2, respectively.

Although the above energy harvesting devices showed good output performance, their resonant frequencies are much higher than the ultra-low-frequency ambient vibrations, which are known for their random and irregular nature, typically below 5 Hz and sometimes as low as 1 Hz [8]. According to the basic principles of vibration energy harvesting, if the excitation frequency of the ambient vibration does not align with the resonant frequency of the harvester, the energy harvesting efficiency will experience a notable decrease.

To enhance energy conversion efficiency and power output under low-frequency vibration excitations, researchers have developed various approaches to broaden the operating bandwidth of energy harvesters. The frequency up-conversion (FUC) technique is one of the typical methods that can be used to address the mismatch between the low-frequency excitation and the high resonant frequency of the harvester. The early work by Umeda *et al.* [33] introduced an impact-based frequency up-conversion method and provided fundamental insights into maximizing energy conversion from mechanical impacts to electrical outputs. Drawing inspiration from this idea, many researchers proposed different methods to address this challenge. Edwards *et al.* [34] developed an electromagnetic energy harvester that uses a magnet as the end mass of a cantilever beam with a stopper. It achieved a 91.5 % increase in power output over the frequency range of 3–7 Hz compared to a traditional cantilever beam. Zhang *et al.* [35] proposed an impact-and-rope-driven piezoelectric energy harvester. They showed that their design could achieve a bandwidth ranging from 2.5 to 10 Hz by adjusting the rope length. Tan *et al.* [36] developed a magnetostrictive energy harvester to convert ultra-low frequency energy from human walking into electricity through a two-stage frequency up-conversion. The magnetostrictive energy harvester achieved a maximum output of 10.06 V and 31.30 mW, sufficient to power 100 LEDs. Fan *et al.* [37] designed an inertial nonlinear piezoelectric energy harvester to be installed in a shoe. Their experiments showed that the power output of the harvester increased from 0.03 to 0.35 mW as the walking speed increased from 2 to 8 km/h.

However, the frequency up-conversion technique may produce high-frequency noises [34,38], result in large mechanical damping [39], and reduce energy conversion efficiency [40]. Therefore, many other researchers focused on developing nonlinear energy harvesters. These nonlinear harvesters can significantly broaden the frequency bandwidth and, in some cases, enhance the response amplitude [41,42]. Upadrashta *et al.* [43] designed an array of nonlinear piezo-magnetoelastic harvesters. Each harvester comprises two piezoelectric cantilevers with tip magnets and can achieve an effective bandwidth of 3.3 Hz, producing a power output of 100 μW when subjected to a harmonic excitation of 2 m/s^2. Yang *et al.* [44] presented a hybrid design that combines bistability and internal resonance for broadband vibration energy harvesting. Because of the internal resonance phenomenon, the system's response exhibited two frequency curves bending in opposite directions on the frequency response graph. As a result, the operating bandwidth of the harvester was doubled compared to other bistable harvesters without internal resonances. Although numerous researchers have proposed various methods to address the frequency mismatch issue, most existing energy harvesters can still only operate within an excitation frequency range of 2–10 Hz [35–37]. When faced with ultra-low frequency excitations, such as human motions, these harvesters produce low power outputs and have poor energy harvesting efficiency. Therefore, it is crucial to design energy harvesters capable of efficiently harnessing ultra-low-frequency excitations with superior conversion efficiency and high-power density.

In this paper, we present a catapult mechanism-enabled push-button energy harvester (CMPEH) designed to efficiently capture ultra-low frequency motion and convert it into electrical energy. Unlike conventional designs, the CMPEH utilizes a unique catapult mechanism that transforms small, ultra-low frequency excitations into rapid, amplified motion of a magnet array. This innovative design uses a simple yet effective structure to achieve high energy output. The high efficiency of this energy harvester is proven and demonstrated through theoretical analysis and experimental validation. The finite element (FE) simulation offers insights into the magnet arrangement and predicts performance. Experimental results validate the capability of the harvester to generate notably high voltage and power outputs. Two demonstration applications showcase the potential of the harvester to sustainably power a variety of low-power electronic devices, highlighting the feasibility of deploying self-powered systems by harnessing ambient ultra-low frequency motions.

2. Structure design and working principle

2.1. Structure and mechanism

The designed push-button energy harvester shown in Fig. 1 consists of a motion conversion unit and an energy conversion unit. The motion conversion unit transforms vertical motion into axial motion, primarily through a button mechanism designed to capture vertical excitations. The top lid is assembled with the bottom lid, forming the framework of the motion conversion unit to house sliders and other components. Pressing the button causes the two sliders to move between the top and bottom lids, allowing vertical motion to be converted into axial motion. Two miniature springs are positioned in the groove of the bottom lid, and this setup supports two limit blocks, which are used to constrain the movement of the sliders. The limit blocks are made of iron

thus, they can be magnetized by the magnet array in the energy conversion unit. The magnet array can only attract the limit block on its adjacent side due to distance limitations, while the limit block on the other side remains unaffected. This setup guarantees that each excitation results in the lateral displacement of the slider on just one side.

In the energy conversion unit, kinetic energy is converted into electricity via electromagnetic induction. When the button is pressed, the lateral displacement of the slider on one side causes the corresponding torsion arm to rotate, which in turn rotates the torsion spring and pushes the magnet array to the left/right side. In the meantime, the two springs that connect the magnet array to the bottom case are being compressed, and potential energy is stored in the buffer springs.

It is noteworthy that the magnet array is supported by small ball bearings to minimize the mechanical energy loss in this process. When the button is pressed past a certain point, the torsion arm rotates at a significantly large angle, unable to withstand the reaction force from the side buffer springs acting on the magnet array. This causes the magnet array to be released, with the potential energy stored in the buffer springs transformed into the kinetic energy of the magnet array. The overall process resembles a catapult launching a projectile. As coils are installed beneath the sideway of the magnet array, electromotive forces will be induced, and voltage outputs will be produced. The magnets within the array are strategically arranged in an S-N-S pole configuration to increase the magnetic flux change rate. The generated AC voltage is converted into DC through a rectifier bridge, further regulated by an energy management circuit, and stored in a capacitor. The stored energy can then be efficiently utilized to power electrical devices such as lamps, LEDs, and sensors.

Fig. 2**(a)** depicts the mechanical modulation and electromechanical conversion processes in the CMPEH. In the initial state, as shown in Fig. 2**(a) i**, the magnet array is locked between the torsion arm and the buffer springs on the right-hand side. The magnet array attracts the nearby limit block (see Fig. 1 for a detailed view) in the motion conversion unit, compressing the miniature spring into the groove on the bottom lid. The two sliders in the motion conversion unit tend to move outward in response to vertical excitation. However, the limit block on the left side, located far away from the magnet array, experiences minimal influence from the magnetic force and, thereby, cannot enter the groove on the bottom lid. Consequently, only the slider on the right side, close to the magnet array, is able to move out, thus completing the motion conversion as shown in Fig. 2**(b) i**. The slider then pushes the torsion arm, causing it to rotate. This rotation movement displaces the magnet array, resulting in the compression of the right-hand side buffer springs and the conversion of external excitation into elastic potential energy stored in buffer springs, as shown in Fig. 2**(a) ii**. When the magnet array is pushed to the critical position, the torsion arm is unable to maintain its grip on the catch of the magnet array.

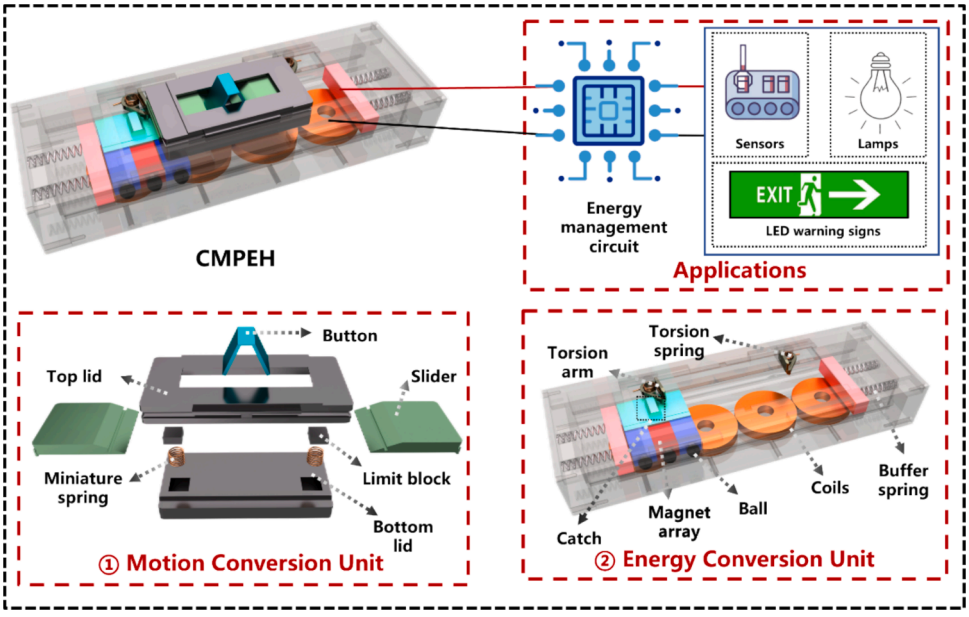

Fig. 1. The schematics showcase the key components of the proposed catapult mechanism-enabled push-button energy harvester (CMPEH).

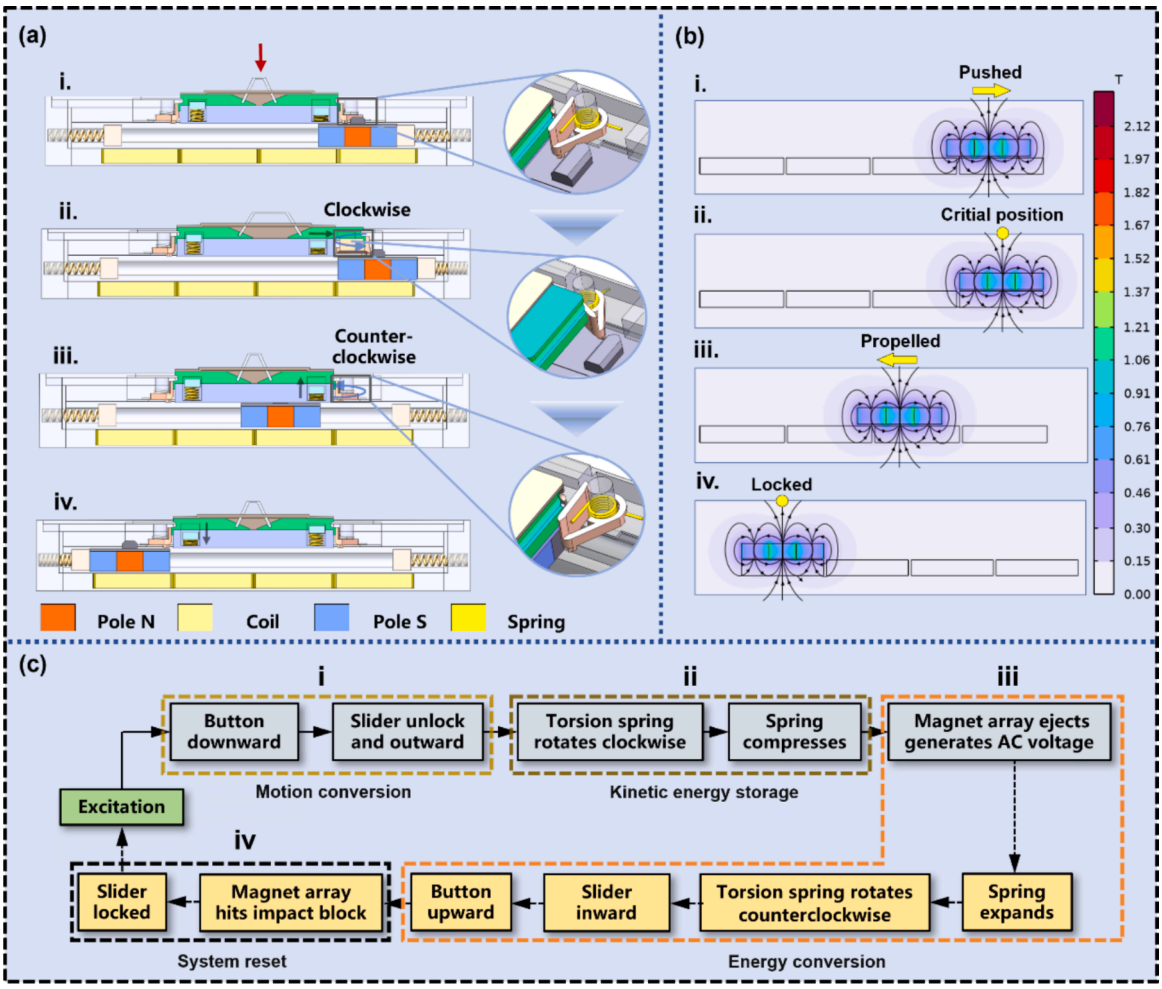

Fig. 2. (a) Mechanical modulation and electromechanical conversion processes in the CMPEH (b) the magnetic field distribution of the magnet array in each state, (c) the flowchart illustrates the different operation states of the CMPEH aligned with Fig. 2(a).

Therefore, the magnet array will be propelled like a projectile as the elastic energy stored in the buffer springs is released. Subsequently, the magnet array will traverse over a set of coils positioned below with an initial velocity, and an induced voltage will be generated in the coils due to the electromagnetic induction phenomenon. As illustrated in Fig. 2**(b) iii**, in the energy conversion stage, the elastic energy stored in the buffer springs is first converted into kinetic energy and then electricity. Meanwhile, it is worth noting that the torsion arm, driven by the torsion spring, rotates back, returning the slider to its original position and resetting the button for the next round of action. Once the magnet array moves to the opposite side, it strikes the impact block, compressing the buffer springs. At this point, the catch on the magnet array is secured by the torsion arm on the left-hand side. Following this, the magnetic force attracts the adjacent limit block into the groove on the bottom lid, unlocking the slider on the same side and resetting the system, as illustrated in Fig. 2**(a) iv** and Fig. 2**(b) iv**. This signifies the completion of one energy harvesting cycle for the CMPEH. The magnetic field distributions of the magnet array, corresponding to the states shown in Fig. 2**(a)**, are plotted in Fig. 2**(b)**. The flowchart in Fig. 2**(c)** succinctly outlines the entire process for ease of understanding and clarity.

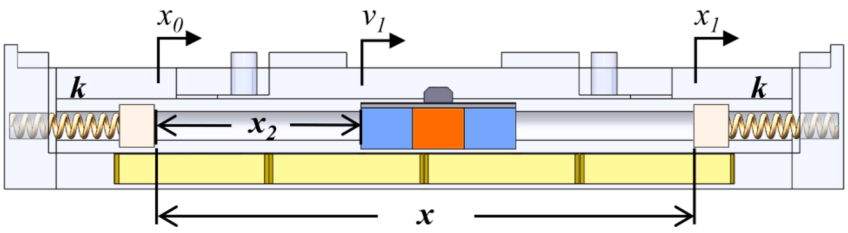

Fig. 3. The simplified lumped parameter model of the moving magnet array.

2.2. Theoretical model

To facilitate the analysis of the motion of the magnet array, which plays a vital role in energy conversion, we developed a simplified lumped parameter model, as shown in Fig. 3. In this model, ***a*** represents the impact block that connects to the side springs, and ***b*** represents the magnet array.

To ensure that magnet array ***b*** can reach the opposite side after being launched from one side propelled by the potential energy released from the side buffer springs, the below condition must be satisfied:

$$\frac{1}{2}k|x_0|^2 \geq C_E v_1(|x|+|x_1|)+E_{loss}+\mu(|x_0|+|x|+|x_1|) \tag{1}$$

where k represents the spring stiffness, x_0 represents the compression of the spring on the left side, x_1 denotes the compression of the spring on the right side, x represents the distance between two impact blocks when their springs are in natural lengths, C_E, and E_{loss}, respectively, stand for the electromagnetic damping coefficient and impact loss, v_1 and μ are the velocity of the magnet array ***b*** and the friction coefficient, respectively. For simplicity, we assume the velocity change of the magnet array ***b*** and the friction is small and negligible thus, v_1 is deemed constant and μ equal to zero.

According to Faraday's law of electromagnetic induction, the induced electromotive force is directly proportional to the magnetic flux change rate, expressed as follows:

$$E = -N\frac{d\varphi}{dt} \tag{2}$$

where E denotes the induced electromotive force, N represents the number of turns in the coil, φ signifies the time-varying magnetic flux, and t denotes time. Since this model considers a planar magnet array moving across coils, the magnetic flux change produced is given by:

$$\varphi = BDx_2 \tag{3}$$

where D denotes the width of the magnet array, B denotes the magnetic field strength, and x_2 represents the distance covered by the magnet array as it moves across the coils. According to the reference [45], the magnetic field strength B of a cubic magnet can be expressed as:

$$B = \left[\frac{B_r}{\pi}arctan\left(\frac{LW}{2z\sqrt{4z^2+L^2+W^2}}\right) - \frac{B_r}{\pi}arctan\left(\frac{LW}{2(D+z)\sqrt{L^2+W^2+4(D+z)^2}}\right)\right] \tag{4}$$

where B_r denotes the remanence field, z represents the distance from a pole face measured along the symmetry axis. L, D, and W are the length, width, and thickness of the magnet array. The force generated through electromagnetic induction can be written as:

$$F = -\frac{N(BD)^2}{R_{inter}+R_{load}}v_1 \tag{5}$$

where R_{inter} represents the internal resistance of the coils and R_{load} denotes the external load. According to the definition of damping, the electromagnetic damping coefficient can be expressed as:

$$C_E = \frac{F}{v_1} \tag{6}$$

By substituting Eqs. (4)–(5) into Eq. (6), one obtains:

$$C_E = -\frac{\left[ND^2\left(\frac{B_r}{\pi}arctan\left(\frac{LW}{2z\sqrt{4z^2+L^2+W^2}}\right) - \frac{B_r}{\pi}arctan\left(\frac{LW}{2(D+z)\sqrt{L^2+W^2+4(D+z)^2}}\right)\right)^2\right]}{R_{inter}+R_{load}} \tag{7}$$

According to the reference [46], the impact loss can be expressed as:

$$E_{loss} = \frac{1}{2}\left(\frac{m_1m_2}{m_1+m_2}\right)\Delta v \tag{8}$$

where m_1 represents the mass of the magnet array, m_2 is the mass of the impact block, and Δv is the relative velocity of the two objects

just before the impact. Substituting the measured data listed in Table 1 into Eqs.(7)-(8), one obtains that $C_E = 0.0841 \times 10^{-3}$N/(m/s), $E_{loss} = 1.227 \times 10^{-3}$ J. Subsequently, substituting Eqs.(7)-(8) into Eq.(1), the minimum compression of the spring on the left side can be derived as:

$$\frac{1}{2}k|x_0|^2 \geq \frac{-ND^2v_1(|x|+|x_1|)}{R_{\text{inter}}+R_{\text{load}}}\left(\frac{B_r}{\pi}\left[\begin{array}{c}\arctan\left(\dfrac{LW}{2z\sqrt{4z^2+L^2+W^2}}\right)\\ -\arctan\left(\dfrac{LW}{2(D+z)\sqrt{L^2+W^2+4(D+z)^2}}\right)\end{array}\right]\right)^2+\frac{1}{2}\left(\frac{m_1m_2}{m_1+m_2}\right)\Delta v \tag{9}$$

Then, by substituting the remaining data into Eq.(9), we can obtain that when the spring compression $x_0 > 1.590$ mm is applied, the magnet array can be propelled to the opposite side. This parameter provides us with guidelines for designing the torsion arm, which directly pushes the magnet array and compresses the side buffer springs.

2.3. Finite element model

This section presents a finite element model (FEM), as shown in Fig. 4**(a)**, built in ANSYS Maxwell to simulate and predict the output performance of the proposed energy harvester, the materials used in the simulation are listed in Table 1. The FEM model assumes an ideal environment where external factors such as air resistance and frictional losses are neglected. The magnet array in the FEM model consists of three magnets with magnetic poles arranged alternately in the order of N-S-N. The movement direction of the magnet array is set along the Y-axis, and the speed is set at 1367 mm/s. Each coil is configured with 3220 turns and an internal resistance of 290 Ω, as identified in the experiment. The material properties of the magnets are checked with the supplier and taken from the standard material library provided by ANSYS Maxwell. These simulation assumptions and parameter settings are intended to ensure result reproducibility while acknowledging potential deviations due to real-world environmental factors.

As illustrated in Fig. 4**(b)**, the magnetic field lines run from the N poles of the magnets situated on the two sides of the array and enter the S pole of the central magnet, forming two distinct closed magnetic loops. This configuration leads to two notable magnetic phase changes in the magnetic flux density (MFD) measurement, as shown in Fig. 4**(c)**. The two magnetic phase changes occur at Y = 10 cm and Y = 20 cm, separated by the width of the magnet. According to Faraday's law, the induced electromotive force is proportional to the change rate of the magnetic flux. Notably, the change in magnetic flux is approximately 1.29 T at the points where the magnetic phase change occurs, implying that the induced voltage will reach the maximum peak at these points.

The induced voltages in the four coils obtained from the simulation are presented in Fig. 4**(d)**. The maximum peak-to-peak voltage that can be produced is about 33.69 V. The voltage peak is generated when the magnetic phase change takes place. Coils #1 and #4 each exhibit a single positive and negative peak, whereas coils #2 and #3 display two positive and two negative peaks. This is because when the magnet array passes over, coils #1 and #4 only experience one magnetic phase change, and coils #2 and #3 encounter two changes. Therefore, we can easily infer that more energy can be harvested from coils #2 and #3.

3. Results and discussion

3.1. Prototype and experimental setup

To evaluate the actual performance of the proposed CMPEH, a prototype with dimensions of 16.25 cm × 5.48 cm × 3.55 cm was built for experimental testing. The whole structure and detailed views of the prototype are shown in Fig. 5**(a)–(c)**. The button is made of manganese steel, the torsion arms are made of titanium alloy, and the frames are fabricated using 3D printing technology. More detailed physical properties and material parameters are listed in Table 2. During the test, the CMPEH was fixed on a frame attached to the vibration test platform. A laser vibrometer sensor (SOPTOP LV-S01) was used to measure the velocity and displacement of the magnet array. The voltage output was gauged by an oscilloscope (RIGOL DHO 1104). The experimental setup is shown in Fig. 5**(d)**.

3.2. Preliminary parametric study

This section investigates the effects of different system parameters, such as the spring stiffness, on the performance of the CMPEH. Since the coils remained unchanged in the tests, we chose coil #2 to focus on its output performance for the subsequent parametric study. Fig. 6 illustrates the voltage responses and charging characteristics of coil #2 when the CMPEH uses different springs ($k = 0.29$ N/mm, 0.49 N/mm, and 0.98 N/mm). Fig. 6**(a)** shows that as the spring stiffness increases from 0.29 N/mm to 0.98 N/mm, the peak

Table 1
The parameters of materials used in ANSYS Maxwell simulation.

Materials	Relative Permeability	Bulk Conductivity (S/m)	Magnetic Coercivity (A/m)	Internal resistance (Ω)
Copper	0.99991	5.8 × 10^7	0	290
NdFe52N (N-pole)	1.47	625000	−730000	/
NdFe52S (S-pole)	1.47	625000	−730000	/
Vacuum	1	0	0	/

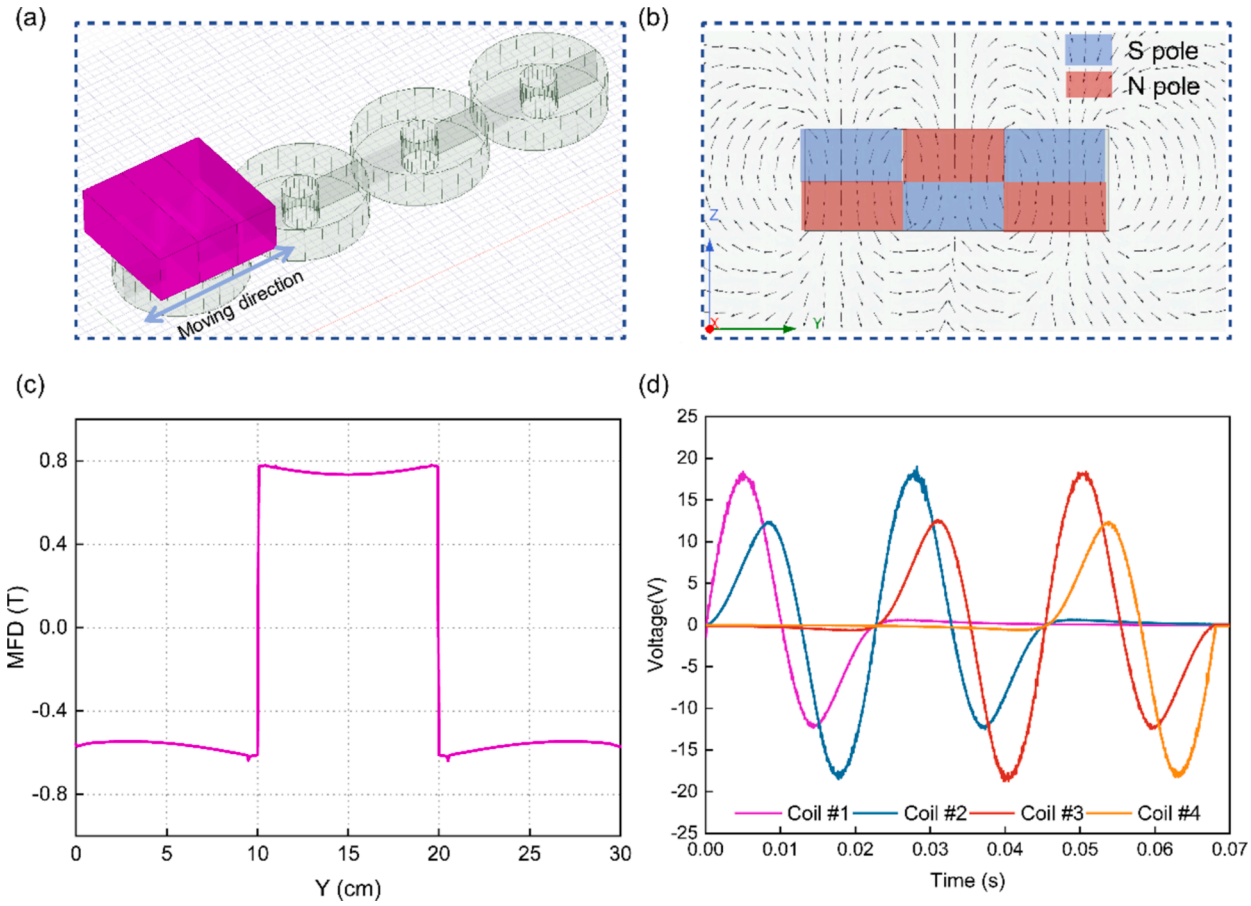

Fig. 4. (a) The finite element model (FEM) of the magnet array and coils in Maxwell simulation, (b) the magnetic field distribution around the magnet array, (c) the magnetic flux density (MFD) along the Y axis of the magnet array, (d) the simulation result of the induced voltages in the four coils.

voltage of the coil rises from 7.6 V to 15.5 V, and the duration for the magnet array to pass over the coil decreases from 0.113 s to 0.053 s. It is well known that the induced voltage is proportional to the change rate of magnetic flux. As the spring stiffness has a notable effect on the speed at which the magnet array passes over the coil, using springs with higher stiffness results in higher induced voltage.

To further assess the energy harvesting performance of the coil under different spring stiffness settings, a capacitor (220 μF) charging test was conducted, and the charging curves were recorded. These results are presented in Fig. 6**(b)** and **(c)**. As the spring stiffness increases from 0.29 N/mm to 0.98 N/mm, the saturation voltage of the 220 μF capacitor increases from 2.46 V to 4.01 V. Moreover, as can be found in Fig. 6**(b)**, the time taken to reach saturation voltage decreases significantly with a higher spring stiffness. This corresponds to the observation in Fig. 6**(a)**.

To better determine the optimal spring stiffness, we calculated the corresponding charging power and energy in charging a 220 μF capacitor. The charging energy can be calculated as:

$$E = \frac{C(U_t - U_0)^2}{2} \tag{10}$$

where E, C, U_t, U_0 represent the charging energy, the capacitance, and the final and initial voltages of the capacitor after and before the charging test, respectively. The formula for calculating the charging power is as follows:

$$P = \frac{E}{t_c} \tag{11}$$

where t_c represents the charging time. The results are presented in Fig. 6**(c)**. With an increase in spring stiffness, the charging power and energy curves exhibit noticeable upward trends. This indicates that higher spring stiffness enhances the performance of the CMPEH. In particular, the optimal performance is observed at a spring stiffness of 0.98 N/mm among the tested casesits charging power is 34.61 mW, and the charging energy reaches 1.82 mJ. Therefore, we chose the spring with a stiffness of 0.98 N/mm for the following experiments.

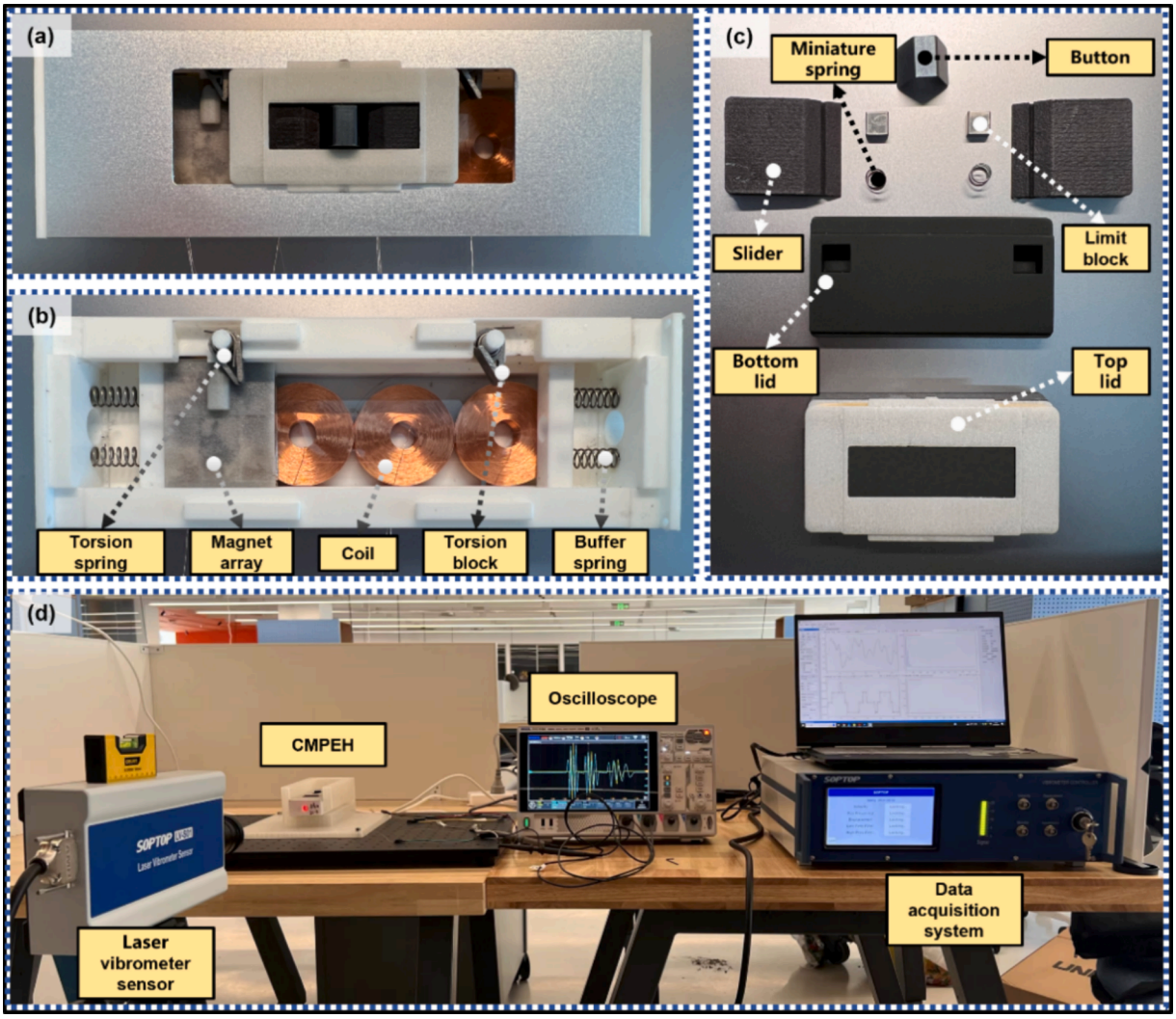

Fig. 5. (a) The whole structure of the proposed CMPEH, (b) the inner view, (c) the components of the motion conversion unit, (d) the experiment setup for conducting measurements.

3.3. Detailed process analysis

This section presents the analysis of the working process of the CMPEH with a spring stiffness of 0.98 N/mm. Fig. 7**(a)** and **(b)** show the open-circuit voltage outputs of the 4 coils, as well as the velocity and displacement of the magnet array. We classify the voltage generation process into three stages based on the magnet array movement.

Stage I – Potential energy storage, Stage II – Magnet array ejection, and Stage III – Magnet array oscillation. In Stage I, the harvester is subjected to vertical excitation, driving the torsion arm to push the magnet array and convert kinetic energy into elastic potential energy stored in the torsion springs. The magnet array remains mostly stationary during this stage, steadily accumulating potential energy in preparation for the subsequent motion phase. The voltages induced in the coils are minimal in this stage, as shown in Fig. 7**(a)**.

In Stage II, the release of the stored potential energy in the compressed buffer springs launches the magnet array like a projectile. The magnet array sequentially induces voltages in coils #1 to #4 during this process. As revealed in Fig. 7**(a)**, the peak voltage for each coil occurs during the magnet's phase transition, aligning with our previous analysis. Specifically, coil #2 generates the highest peak-to-peak voltage of 40.54 V, coils #1, #3, and #4 produce 36.01 V, 35.47 V, and 28.68 V, respectively. In addition, the velocity of the magnet array exhibits a three-phase decline in Stage II, dropping from 1.68 m/s to 1.23 m/s. This decrease in speed is a result of the attraction forces exerted by the limit blocks located on the two sides of the bottom lid. At the beginning and end of the motion, only one limit block on one side exerts the attractive force, whereas, in the middle, both blocks attract the magnet array, leading to a more rapid deceleration.

After Stage II, the magnet array is captured and halted by the torsion arm on the opposite side. Despite the impact of the opposite

Table 2
Detail physical properties and material parameters.

Component	Unit/Specification	Values
CMPEH	Dimensions (cm)	16.25 × 5.48 × 3.55
Button	Dimensions (cm)	13.2 × 10.1 × 9.2
	Young's modulus (GPa)	200
Torsion spring	Model	UA90L5 − 5–0.6, UA90R5 − 5–0.6
Spring	Stiffness (N/mm)	0.29, 0.49, 0.98
	External diameter (mm)	18.6
	Free length (mm)	25
Magnet	Number	3
	Magnet grade	N52
	Material	Neodymium
Magnet array	Length L (mm)	30
	Width D (mm)	30
	Thickness W (mm)	6
	B_r (T)	0.3
	Weight (g)	53
Coils	Number	4
	Outer diameter (mm)	30
	Inner diameter (mm)	8
	Turns	3220
	Wire diameter (mm)	0.12
	Internal resistance (Ω)	290
Impact block	Material	PLA
	Weight (g)	3

spring at a speed of around 1.2 m/s, it generates significant impact force, leading to the oscillation of the magnet array. The oscillation of the magnet array leads to coils #3 and #4 continuing to 'cut' the magnetic field lines, generating induced voltage, as depicted in Stage III of Fig. 7**(a)**. Throughout this stage, the oscillation of the magnet array gradually slows down until it eventually reaches a standstill due to the damping phenomenon, causing the induced voltage to decrease back to zero.

Fig. 7**(c)–(f)** compare the experimental voltage responses of each coil (coil #1 to #4) with the simulation results from ANSYS Maxwell. In the initial phase, the elastic potential energy stored in the spring array is rapidly released and transformed into the initial kinetic energy of the magnet array, resulting in a high initial speed. This leads to significant voltage peaks in the responses of coils #1 and #2, as shown in Fig. 7**(c)** and **(d)**. As the magnet array slows down, the experimental voltage response gradually decreases, aligning closely with the characteristics predicted by the simulation results.

At the end of the final phase of the magnet array's motion, additional oscillations appear in the responses of coil # 3 and #4, as observed in experimental results in Fig. 7**(e)** and **(f)**. These oscillations arise from the mechanical vibrations generated by the collision between the magnet array and the impact block. As a result, the magnet array keeps cutting the magnetic field lines, leading to continued oscillations in the voltage response. This phenomenon is consistent with previous analyses, which suggested that collision effects significantly influence the voltage responses of coils #3 and #4. Since this collision was not included in the simulation, the simulation results cannot capture the oscillations in the final phase. This limitation is due to the simplifications implemented in the simulation modeling. Many factors, such as friction, air resistance, material inhomogeneities, and loose connections, may introduce unexpected energy losses and affect dynamic oscillations in actual tests. Unfortunately, these factors are too complicated to identify and be accounted for in the simulation.

3.4. The power output performance

This section details a series of experiments conducted to further investigate the optimal output performance of the developed CMPEH. Firstly, the circuit shown in Fig. 8 is utilized, with switches S1, S2, S3, and S4 set on while the others off to assess each coil's power output under different external resistances. Spring stiffness is set as 0.98 N/mm.

Fig. 9**(a)** plots the RMS power outputs of the four coils as a function of the external resistance. All four coils exhibit similar trend characteristics when subjected to the same excitation condition, as their peak-shaped curves show. As the resistance increases, the output power of a coil initially rises to a peak value before gradually decreasing to a negligible level with further increases in the external resistance. The maximum power output is attained when the load impedance matches the internal impedance. This relationship can be represented in the following formula for purely resistive circuits:

$$P_{max} = \frac{V^2}{R_{inter} + R_{load}} \tag{12}$$

where P_{max}, V, R_{inter}, R_{load} represent the maximum power, voltage, internal resistance and external resistance, respectively.

By shunting coil #2 to an external resistance of 290 Ω, it achieves its peak RMS power output of 32.23 mW. At the same resistance of 290 Ω, the other coils also achieve their respective maximum RMS power outputs, coil #4 attains 10.91 mW, coil #3 produces 23.12

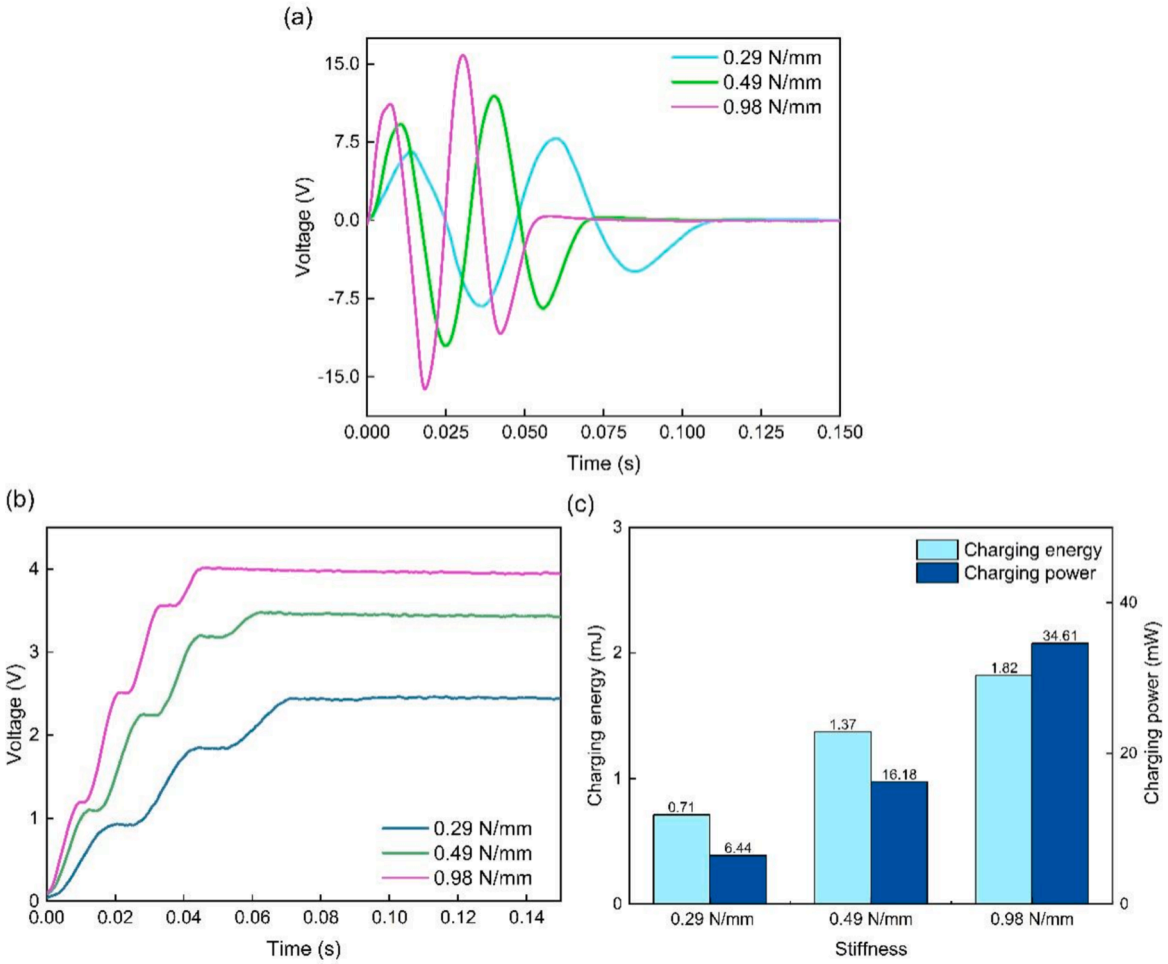

Fig. 6. (a) The voltage responses when using springs with different stiffnesses (k = 0.29 N/mm, 0.49 N/mm, 0.98 N/mm), (b) the charging curve of the 220 μf capacitor under different spring stiffness settings (k = 0.29 N/mm, 0.49 N/mm, 0.98 N/mm), (c) the calculated charging power and energy (k = 0.29 N/mm, 0.49 N/mm, 0.98 N/mm).

mW, and coil #1 generates 22.12 mW. The external load at which each coil attains its peak power corresponds to the resistance characteristics of the coils, reinforcing the theoretical prediction that the coils would achieve maximum power outputs at this point.

Subsequently, to further quantify the charging performance of the prototyped CMPEH, we conducted tests to examine the saturation voltage and average charging power profiles of different capacitors when charged with our CMPEH. In the tests, we set switch S5 on and the others off. Then, we tested four different capacitors 220 μF, 470 μF, 680 μF, and 1000 μF. Fig. 9**(b)** shows the voltage rising curves when charging different capacitors under the same excitation condition. These curves demonstrate a pronounced stepwise ascent, where each peak in voltage corresponds to the emergence of a distinct step in the curve. The data shows a decline in terminal voltage from 8.06 V for the 220 μF capacitor to 3.04 V for the 1000 μF capacitor, along with an increase in the time needed to achieve a stable voltage. Specifically, the terminal voltages for the 470 μF and 680 μF capacitors are, respectively, 5.10 V and 3.94 V.

The charging power and energy are demonstrated and compared in Fig. 9**(c)**. The 220 μF capacitor displayed the highest energy and power output at 7.16 mJ and 89.48 mW, respectively. With an increase in capacitance to 470 μF, 680 μF, and 1000 μF, there was a notable decline in both the charging energy and power. The corresponding energy, power, and calculated volume power densities are listed in Table 3. Table 4 presents a comparison of the proposed CMPEH and some other low-frequency energy harvesters reported in the literature. The table highlights several key parameters, including the volume, excitation characteristics, average power output, and volume power density, which are crucial for assessing the performance and efficiency of an energy harvester. Our prototyped CMPEH has a volume of 315.70 cm^3, which is moderate compared to other harvesters. Nevertheless, it produces an average power output of 76.370 mW and a power density of 241.920 W/m^3, positioning it as the most efficient design in terms of power density. This high power density is due to the catapult mechanism employed. Another remarkable feature of the CMPEH is its ultra-low operational frequency range. Unlike other harvesters that operate at high frequencies, the CMPEH can effectively capture ultra-low-frequency vibrations below 1 Hz. This capability makes it particularly suited for a variety of real-world applications, offering a promising solution for efficiently harvesting energy from low-frequency and intermittent motion sources. However, the CMPEH also has certain

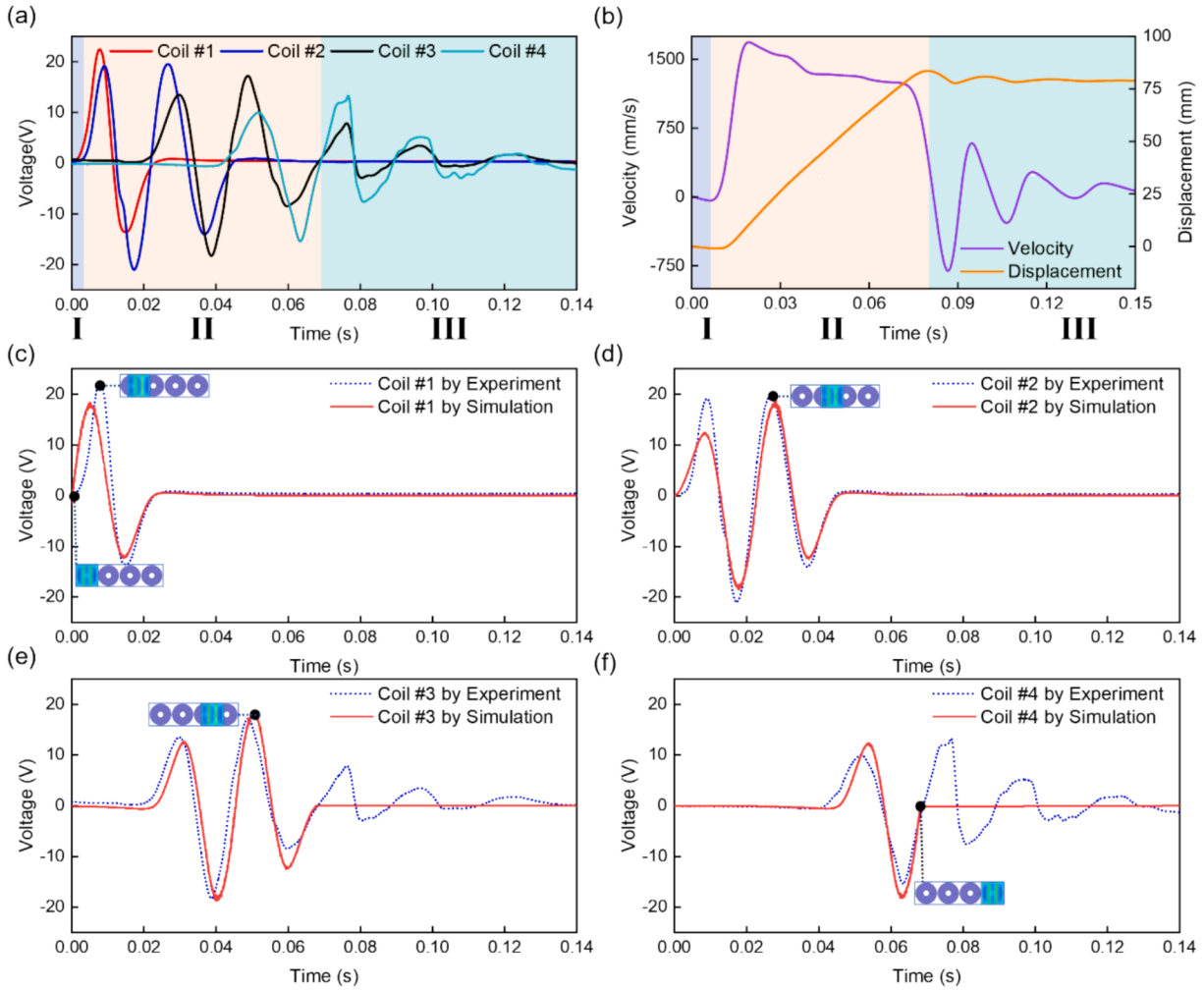

Fig. 7. (a) Open-circuit voltages induced in the coils when the CMPEH uses the spring stiffness of 0.98 N/mm, (b) the time-history velocity and displacement of the magnet array during a single operational cycle, (c)-(f) the comparison between the simulated and experimentally obtained voltage responses of Coil #1 to #4.

limitations. Due to the employed mechanism, it necessitates a relatively long reset time (about 0.15 s), making it unsuitable for high-frequency (>5 Hz) operations. Additionally, the mechanical components require further investigation to enhance their structural durability and performance stability under long-term repetitive usage. Future research could focus on improving this design by addressing the two aforementioned issues, thereby expanding its practical applications across a wider range of scenarios.

4. Practical applications

4.1. Lighting up LEDs

In this subsection, to showcase the potential of the prototyped CMPEH for real applications, we first designed an experiment to light up LEDs. In this experiment, we activated switch S6 in the circuit shown in Fig. 8 with the other switches turned off. The applied excitation was the same as depicted in Section 3.4. We built an LED array consisting of 4500 LEDs, as shown in Fig. 10**(a)**. Each LED bulb operates at a voltage of 1.6 V and consumes a power of 0.06 W, emitting red light when illuminated. The LED array was successfully lit up by the prototyped CMPEH, as shown in Fig. 10**(b)**. To visualize the LED lighting process, we used an oscilloscope to record the terminal voltage across the LED array, and the result is presented in Fig. 10**(c)**. The voltage fluctuations observed correspond to the blinking process of the LEDs. When the terminal voltage is greater than 1.6 V, the LED array lights up. Fig. 10**(d)** showcases the LED array brightly lit and arranged to spell out 'HKUSTGZ SMS LAB', which is the abbreviation for Hong Kong University of Science and Technology (Guang Zhou) Smart Materials & Structures Laboratory. A video showcasing the lighting-up process of the 4500 LEDs can be found in Video S1.

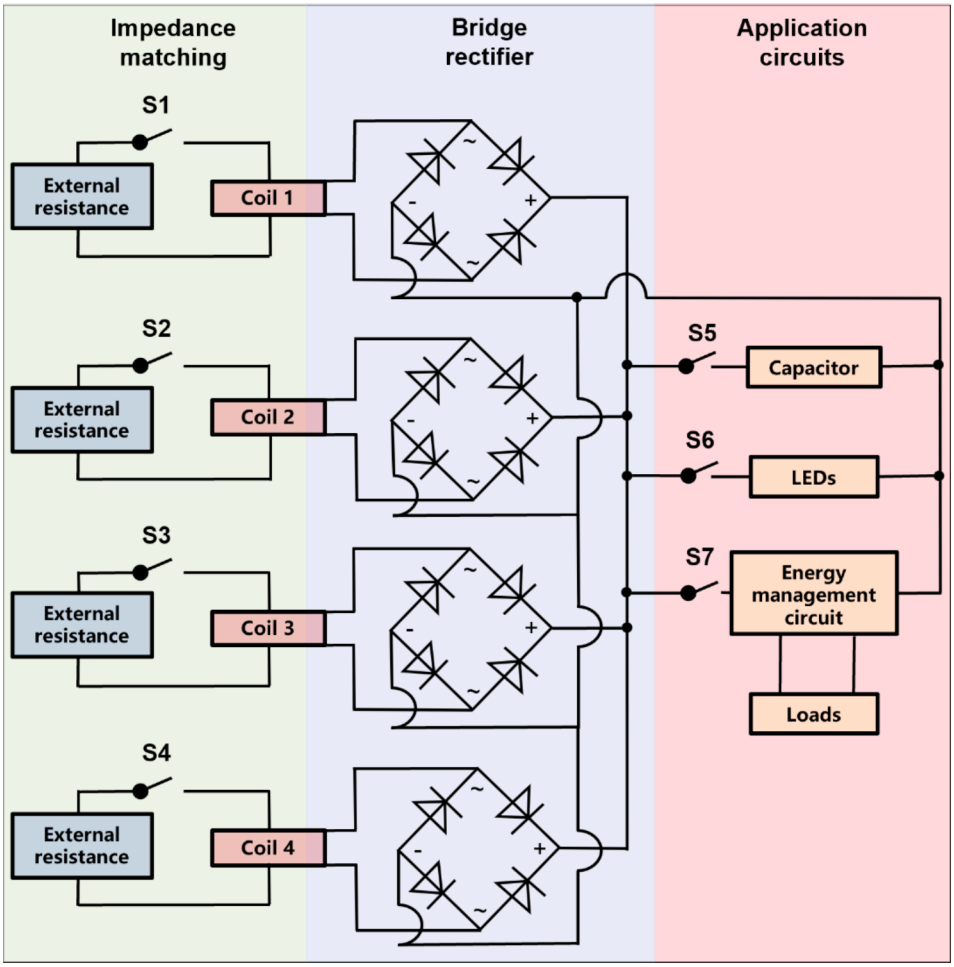

Fig. 8. The testing circuit to evaluate the proposed CMPEH.

4.2. *Powering electronic devices*

We then further demonstrated the potential of the CMPEH by using it to power electronic devices. In the application demonstration, a temperature & humidity sensor (model SHT4x), as shown in Fig. 11**(a)**, was utilized as the device. Using the circuit shown in Fig. 8, we turned on switch S7 while leaving the other switches off. The energy management module was developed using the commercial chip LTC-3588, and a 220μF capacitor was used as the energy storage capacitor at its input end. A detailed schematic of the energy management circuit is shown in Fig. 11**(b)**. The excitation applied to the CMPEH remained consistent with that described in Section 3.4. The real-time terminal voltages across the energy storage capacitor (ESC) and energy management circuit (EMC) are shown in Fig. 11**(d)**.

In stage I, the CMPEH receives the excitation, converts mechanical energy into electricity, and initiates the charging process of the energy storage capacitor. The terminal voltage of the capacitor rises to 7.89 V. When the terminal voltage of the capacitor exceeds 4.73 V, the energy management module starts to output a stable 3.6 V DC voltage. In stage II, the capacitor supplies the energy required to power the SHT4x sensing module. The sensor refresh interval is configured to 3.5 s, with each refresh depleting stored energy, leading to a decline in the ESC voltage. Despite this, the EMC voltage remains constant, demonstrating effective regulation by the energy management module. After seven refreshing cycles, accurate temperature and humidity readings are acquired and displayed on the screen. After that, the remaining energy is adequate to sustain the sensor for one more refresh. In stage III, when the terminal voltage of the ESC falls below 4.73 V, a notable voltage drop occurs, leading to the cessation of operation of the SHT4x sensing module.

The experiment demonstrated that a single excitation is sufficient for the sensor to function successfully. It is anticipated that, when exposed to continuous ultra-low frequency excitation, this energy harvester has the potential to entirely supplant the sensor battery as its primary power source. Overall, the experimental results prove that the output performance of this energy harvester can effectively enable real-time self-powered passive environmental monitoring.

The experiment demonstrated that a single excitation is sufficient to activate the temperature sensor successfully. Additionally, according to the harvested energy, it can be easily estimated that it can power many IoT devices. The experimental results have proven

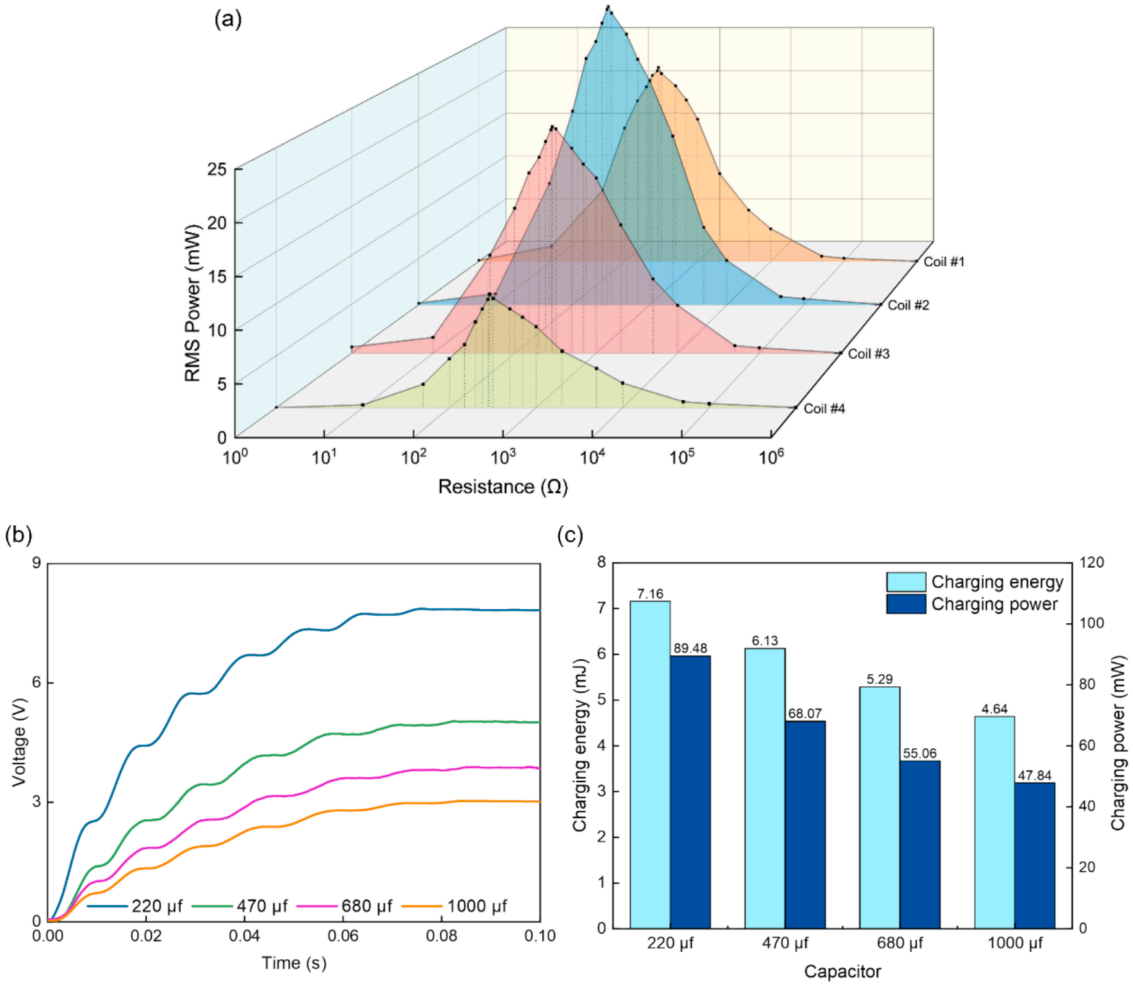

Fig. 9. (a) The power output of the four coils under different resistances, (b) recorded voltage curves, (c) charging energy and power when charging different capacitors.

Table 3
The saturation voltage, charging energy, power, and volume power density when charging different capacitors.

Capacitor	Saturation voltage (V)	Energy (mJ)	Power (mW)	Volume power density (W/m^3)
220 μF	8.06	7.16	89.48	283.43
470 μF	5.10	6.13	68.07	215.63
680 μF	3.94	5.29	55.06	174.42
1000 μF	3.04	4.64	47.84	151.52

the power generation capability of this harvester. In terms of practical applications, this energy harvester can be employed in various scenarios. For instance, it can be embedded beneath floor tiles, leading to a smart flooring system that can sense and collect data on foot traffic as pedestrians walk over it. This technology might be useful in markets and exhibition settings. Moreover, it can be anticipated that the proposed energy harvester could replace a chemical battery as the primary power source, given continuous ultra-low frequency excitation. This transition could unlock a wider range of applications across different fields. In structural health monitoring, for example, the harvester can be implemented in civil infrastructure, such as bridges and buildings, to power sensors that monitor strain, displacement, and vibrations induced by environmental loads, allowing for real-time monitoring without the need for external power supplies. Furthermore, the proposed energy harvester can be utilized in railway systems to harness slow periodic vibrations from tracks or suspension systems to power condition-monitoring sensors, enabling long-term, battery-free, and maintenance-free operation for structural health assessment. Overall, the above experimental results have confirmed the outstanding output performance of this energy harvester, providing users the opportunity to envision a variety of practical applications.

Table 4
Summary of reported energy harvesters under low-frequency excitations.

Refs	Volume	Excitation characteristics	Average power	Volume power density
Zhu *et al.* [47]	134.69 cm^3	2–5 Hz	0.056 mW	0.412 W/m^3
Fan *et al.* [48]	52.42 cm^3	0.5–5 Hz	0.280 mW	5.350 W/m^3
Zou *et al.* [49]	5500.00 cm^3	Pedestrian (65 kg)	54.000 mW	98.180 W/m^3
AYin *et al.* [50]	75.25 cm^3	1.5–4 Hz	0.980 mW	13.020 W/m^3
Fan *et al.* [51]	21.50 cm^3	1–5 Hz	5.300 mW	246.510 W/m^3
Iqbal *et al.* [52]	46.80 cm^3	8–51 Hz	0.005 mW	0.100 W/m^3
Hou *et al.* [32]	0.13 m^3	< 5 Hz	0.020 mW	0.000134 W/m^3
Thitima *et al.* [53]	0.03 m^3	Pedestrian	520.000 mW	22.500 W/m^3
Liu *et al.* [54]	5280.00 cm^3	5 Hz	7.210 mW	1.360 W/m^3
This work	**315.70 cm^3**	**< 1 Hz**	**76.370 mW**	**241.920 W/m^3**

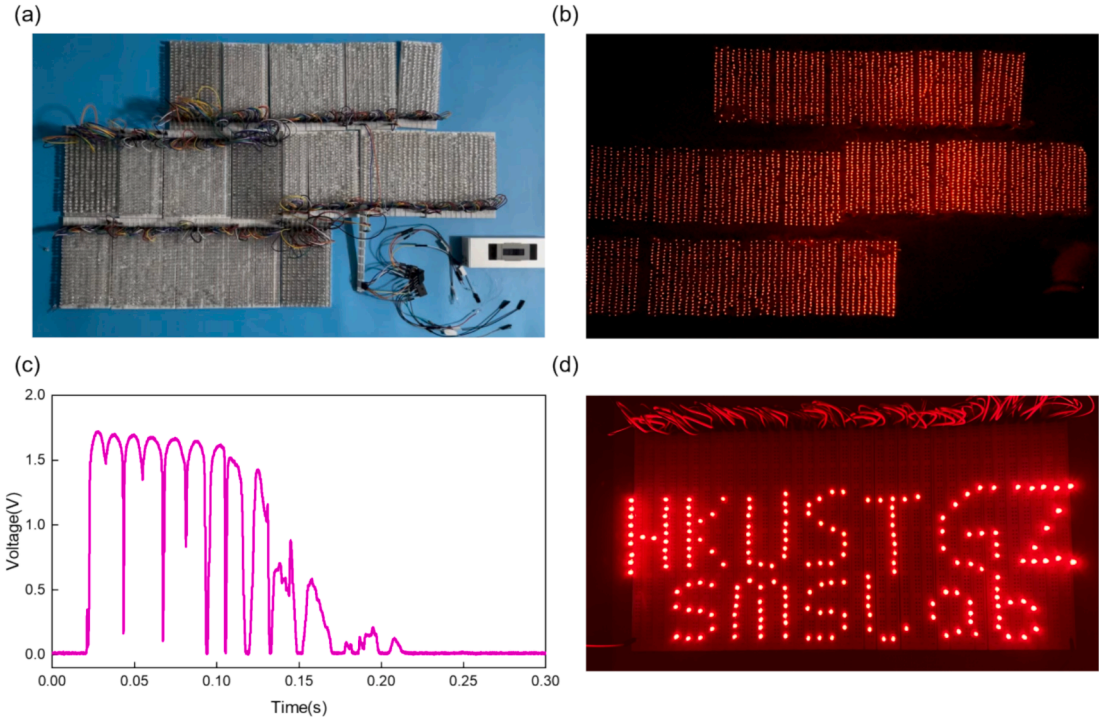

Fig. 10. (a) The LED array consisting of 4500 LED bulbs, (b) the LED array brightly lit, (c) the recorded terminal voltage across the LED array, (d) the illuminated LED array spelling out 'HKUSTGZ SMS LAB'. The lighting-up process of the LEDs can be viewed in a video included in the supplementary files.

5. Conclusions

This paper has presented a catapult mechanism-enabled push-button energy harvester (CMPEH). It can efficiently capture ultra-low frequency motion and convert it into electricity. The CMPEH mainly comprises a motion conversion module and an energy conversion module. The motion conversion module is designed to transform vertical into axial motion, and the energy conversion module utilizes electromagnetic induction to harness electrical energy from the kinetic motion generated by the motion conversion module. A simplified theoretical model has been developed to analyze the kinetic motion of a key component in the CMPEH. Moreover, a simulation model has also been built to predict the voltage output of the CMPEH. Based on the design, we fabricated a prototype and conducted tests to assess its performance. Compared with the existing designs, the proposed CMPEH demonstrates advantages in the following aspects. First, it is small and compact in structure, making it easy to install. Second, it has been demonstrated that the harvester can effectively harvest energy from ultra-low frequency excitations. Specifically, it can generate a peak-to-peak open-circuit voltage exceeding 40 V under single ultra-low frequency excitation (< 1 Hz), with the voltage rising as the spring stiffness increases. Under the same excitation condition, its RMS power output can reach 76.37 mW, indicating a volume power density of 241.92 W/m3. Third, it has been proven that this harvester can sustain low-power sensors, and the energy harvested from a single excitation is sufficient to operate a commercial temperature and humidity sensor. In general, the proposed energy harvester has demonstrated promising potential in harnessing energy from ultra-low frequency excitations. The structural design of the harvester can be further

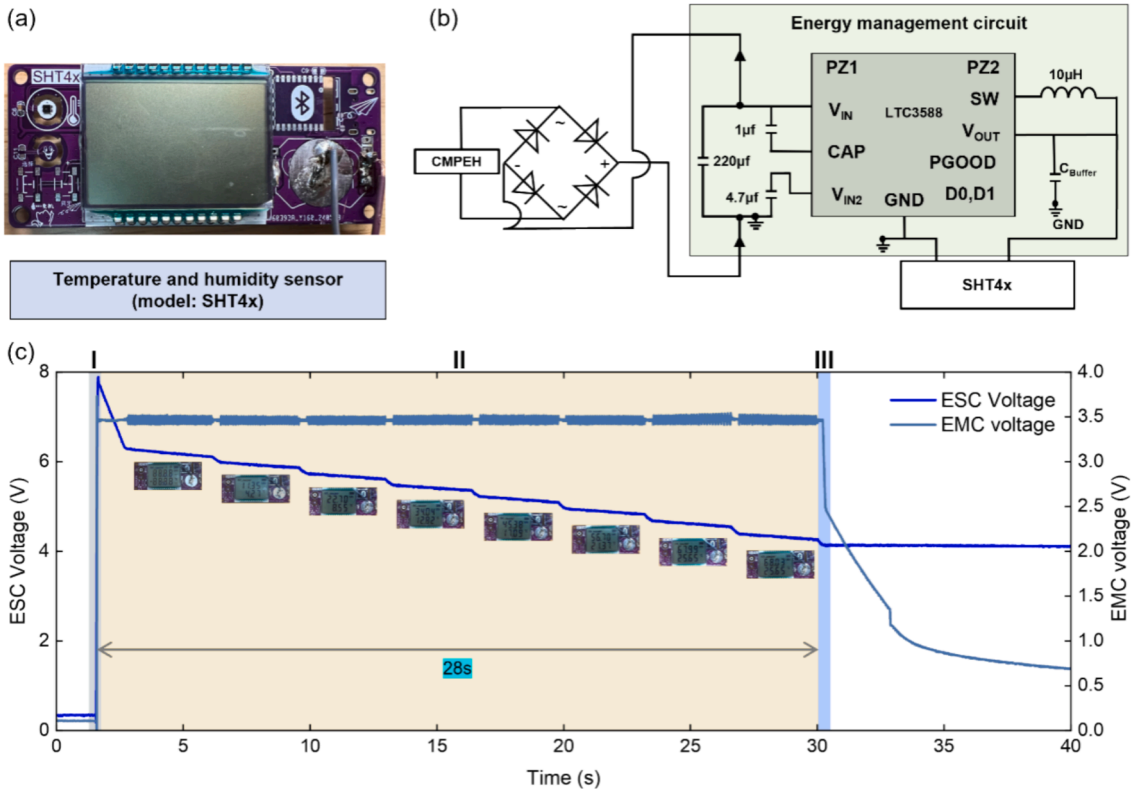

Fig. 11. (a) The temperature and humidity sensor (model. SHT4x), (b) the power supply and energy management circuit, (c) the terminal voltages across the energy storage capacitor (ESC) and the energy management circuit (EMC). A video showing how the sensing module was powered can be found in the supplementary files.

optimized to enhance the performance and adapt to different application requirements.

CRediT authorship contribution statement

Yihao Li: Writing – original draft, Visualization, Validation, Software, Methodology, Investigation, Formal analysis, Data curation. **Xuzhang Peng:** Visualization, Validation, Software, Methodology, Investigation, Formal analysis, Data curation. **Yizhou Li:** Validation, Software, Investigation, Data curation. **Dian Li:** Software, Investigation. **Guobiao Hu:** Writing – review & editing, Supervision, Resources, Project administration, Funding acquisition, Formal analysis, Conceptualization.

Declaration of competing interest

The authors declare that they have no known competing financial interests or personal relationships that could have appeared to influence the work reported in this paper.

Acknowledgments

This work was financially supported by the National Natural Science Foundation of China (Grant No. 52305135), Guangzhou Municipal Science and Technology Project (Grant No. 2023A03J0011), Guangdong Provincial Key Lab of Integrated Communication, Sensing and Computation for Ubiquitous Internet of Things (Grant No. 2023B1212010007), Guangzhou Municipal Key Laboratory on Future Networked Systems (Grant No. 024A03J0623), and Guangzhou Municipal Bureau of Science and Technology (Grant Nos. 2024A03J0533, 2024A04J4448).

Appendix A. Supplementary material

Supplementary data to this article can be found online at https://doi.org/10.1016/j.ymssp.2024.112268.

Data availability

Data will be made available on request.

References

[1] K. Cao, G. Xu, J. Zhou, T. Wei, M. Chen, S. Hu, QoS-adaptive approximate real-time computation for mobility-aware IoT lifetime optimization, IEEE Trans. Comput. Aided Des. Integr. Circuits Syst. 38 (10) (2018) 1799–1810.
[2] B.D. Deebak, F. Al-Turjman, A hybrid secure routing and monitoring mechanism in IoT-based wireless sensor networks, Ad Hoc Netw. 97 (2020) 102022.
[3] M.S. Hossain, G. Muhammad, W. Abdul, B. Song, B.B. Gupta, Cloud-assisted secure video transmission and sharing framework for smart cities, Futur. Gener. Comput. Syst. 83 (2018) 596–606.
[4] Y. Liu, L. Zhang, Y. Yang, L. Zhou, L. Ren, F. Wang, R. Liu, Z. Pang, M.J. Deen, A novel cloud-based framework for the elderly healthcare services using digital twin, IEEE Access 7 (2019) 49088–49101.
[5] A.A. Zaidan, B.B. Zaidan, M. Qahtan, O.S. Albahri, A.S. Albahri, M. Alaa, F.M. Jumaah, M. Talal, K.L. Tan, W. Shir, A survey on communication components for IoT-based technologies in smart homes, Telecommun. Syst. 69 (2018) 1–25.
[6] S. Gohari, R. Adams, M. Ahmed, Q.Q. Liang, N. Moslemi, C. Burvill, Experimental and numerical studies on the vibration-based structural health monitoring of dimpled steel sheets with residual stresses, Eng. Struct. 306 (2024) 117882.
[7] K. Han, K. Huang, Wirelessly powered backscatter communication networks modeling, coverage, and capacity, IEEE Trans. Wirel. Commun. 16 (4) (2017) 2548–2561.
[8] Q. Tan, K. Fan, K. Tao, L. Zhao, M. Cai, A two-degree-of-freedom string-driven rotor for efficient energy harvesting from ultra-low frequency excitations, Energy 196 (2020) 117107.
[9] D. Zhu, Vibration energy harvesting machinery vibration, human movement and flow induced vibration, Sustain. Energy Harvest. Technologies-past, Present and Future 1 (2011) 22–54.
[10] L. Qi, H. Pan, Y. Pan, D. Luo, J. Yan, Z. Zhang, A review of vibration energy harvesting in rail transportation field, Iscience 25 (3) (2022).
[11] J. Wang, L. Geng, L. Ding, H. Zhu, D. Yurchenko, The state-of-the-art review on energy harvesting from flow-induced vibrations, Appl. Energy 267 (2020) 114902.
[12] J. Wang, S. Gu, C. Zhang, G. Hu, G. Chen, K. Yang, H. Li, Y. Lai, G. Litak, D. Yurchenko, Hybrid wind energy scavenging by coupling vortex-induced vibrations and galloping, Energ. Conver. Manage. 213 (2020) 112835.
[13] J. Thiébot, D. Coles, A.-C. Bennis, N. Guillou, S. Neill, S. Guillou, M. Piggott, Numerical modelling of hydrodynamics and tidal energy extraction in the alderney race: a review, Phil. Trans. R. Soc. A 378 (2178) (2020) 20190498.
[14] Y. Zhang, T. Wang, A. Luo, Y. Hu, X. Li, F. Wang, Micro electrostatic energy harvester with both broad bandwidth and high normalized power density, Appl. Energy 212 (2018) 362–371.
[15] K. Fan, M. Cai, H. Liu, Y. Zhang, Capturing energy from ultra-low frequency vibrations and human motion through a monostable electromagnetic energy harvester, Energy 169 (2019) 356–368.
[16] Y. Peng, W. Xu, Y. Gong, X. Peng, Z. Li, Electromechanical coupling of a 3.88 W harvester with circumferential step-size field modeling, validation and self-powered wearable applications, Smart Mater. Struct. 33 (2) (2024) 025039.
[17] Z.-Q. Lu, D. Wu, H. Ding, L.-Q. Chen, Vibration isolation and energy harvesting integrated in a Stewart platform with high static and low dynamic stiffness, App. Math. Model. 89 (2021) 249–267.
[18] Z. Li, C. Xin, Y. Peng, M. Wang, J. Luo, S. Xie, H. Pu, Power density improvement of piezoelectric energy harvesters via a novel hybridization scheme with electromagnetic transduction, Micromachines 12 (7) (2021) 803.
[19] X. Shan, H. Li, Y. Yang, J. Feng, Y. Wang, T. Xie, Enhancing the performance of an underwater piezoelectric energy harvester based on flow-induced vibration, Energy 172 (2019) 134–140.
[20] Z. Li, X. Peng, G. Hu, D. Zhang, Z. Xu, Y. Peng, S. Xie, Towards real-time self-powered sensing with ample redundant charges by a piezostack-based frequency-converted generator from human motions, Energ. Conver. Manage. 258 (2022) 115466.
[21] Z. Li, X. Peng, G. Hu, Y. Peng, Theoretical, numerical, and experimental studies of a frequency up-conversion piezoelectric energy harvester, Int. J. Mech. Sci. 223 (2022) 107299.
[22] G. Hu, L. Tang, A. Banerjee, R. Das, Metastructure with piezoelectric element for simultaneous vibration suppression and energy harvesting, J. Vib. Acoust. 139 (1) (2017) 011012.
[23] G. Hu, L. Tang, J. Liang, R. Das, Modelling of a cantilevered energy harvester with partial piezoelectric coverage and shunted to practical interface circuits, J. Intell. Mater. Syst. Struct. 30 (13) (2019) 1896–1912.
[24] J. Chen, Y. Huang, N. Zhang, H. Zou, R. Liu, C. Tao, X. Fan, Z.L. Wang, Micro-cable structured textile for simultaneously harvesting solar and mechanical energy, Nat. Energy 1 (10) (2016) 1–8.
[25] Z. Li, X. Peng, Y. Peng, J. Luo, S. Xie, H. Pu, Electromagnetic and triboelectric hybrid energy collector for low-frequency movement, Google Patents (2022).
[26] Y. Wang, X. Liu, Y. Wang, H. Wang, H. Wang, S.L. Zhang, T. Zhao, M. Xu, Z.L. Wang, Flexible seaweed-like triboelectric nanogenerator as a wave energy harvester powering marine internet of things, ACS Nano 15 (10) (2021) 15700–15709.
[27] C. Zhao, D. Liu, Y. Wang, Z. Hu, Q. Zhang, Z. Zhang, H. Wang, T. Du, Y. Zou, H. Yuan, Highly-stretchable rope-like triboelectric nanogenerator for self-powered monitoring in marine structures, Nano Energy 94 (2022) 106926.
[28] Y. Wang, Z. Hu, J. Wang, X. Liu, Q. Shi, Y. Wang, L. Qiao, Y. Li, H. Yang, J. Liu, Deep learning-assisted triboelectric smart mats for personnel comprehensive monitoring toward maritime safety, ACS Appl. Mater. Interf. 14 (21) (2022) 24832–24839.
[29] S. Priya, C.-T. Chen, D. Fye, J. Zahnd, Piezoelectric windmill a novel solution to remote sensing, Jpn. J. Appl. Phys. 44 (1L) (2004) L104.
[30] Y. Minami, E. Nakamachi, Development of enhanced piezoelectric energy harvester induced by human motion, IEEE, 2012, pp. 1627–1630.
[31] M. Asadi, R. Ahmadi, A.M. Abazari, Footstep-powered floor tile Design and evaluation of an electromagnetic frequency up-converted energy harvesting system enhanced by a cylindrical Halbach array, Sustain. Energy Technol. Assess. 60 (2023) 103571.
[32] C. Hou, T. Chen, Y. Li, M. Huang, Q. Shi, H. Liu, L. Sun, C. Lee, A rotational pendulum based electromagnetic/triboelectric hybrid-generator for ultra-low-frequency vibrations aiming at human motion and blue energy applications, Nano Energy 63 (2019) 103871.
[33] M. Umeda, K. Nakamura, S. Ueha, Analysis of the transformation of mechanical impact energy to electric energy using piezoelectric vibrator, Jpn. J. Appl. Phys. 35 (5S) (1996) 3267.
[34] B. Edwards, K.C. Aw, A.P. Hu, Mechanical frequency up-conversion for sub-resonance, low-frequency vibration harvesting, J. Intell. Mater. Syst. Struct. 27 (16) (2016) 2145–2159.
[35] J. Zhang, L. Qin, A tunable frequency up-conversion wideband piezoelectric vibration energy harvester for low-frequency variable environment using a novel impact-and rope-driven hybrid mechanism, Appl. Energy 240 (2019) 26–34.
[36] Y. Tan, G. Lu, M. Cong, X. Wang, L. Ren, Gathering energy from ultra-low-frequency human walking using a double-frequency up-conversion harvester in public squares, Energ. Conver. Manage. 217 (2020) 112958.
[37] K. Fan, Z. Liu, H. Liu, L. Wang, Y. Zhu, B. Yu, Scavenging energy from human walking through a shoe-mounted piezoelectric harvester, Appl. Phys. Lett. 110 (14) (2017).
[38] M.A. Halim, J.Y. Park, Piezoceramic based wideband energy harvester using impact-enhanced dynamic magnifier for low frequency vibration, Ceram. Int. 41 (2015) S702–S707.

[39] L. Gu, C. Livermore, Impact-driven, frequency up-converting coupled vibration energy harvesting device for low frequency operation, Smart Mater. Struct. 20 (4) (2011) 045004.
[40] M.A. Halim, H. Cho, J.Y. Park, Design and experiment of a human-limb driven, frequency up-converted electromagnetic energy harvester, Energ. Conver. Manage. 106 (2015) 393–404.
[41] N. Tran, M.H. Ghayesh, M. Arjomandi, Ambient vibration energy harvesters. a review on nonlinear techniques for performance enhancement, Int. J. Eng. Sci. 127 (2018) 162–185.
[42] Z. Guo, S. Jiang, Y. Shen, G. Jiang, B. Xiao, Q. Xu, M. Li, Nonlinear dynamic analysis and vibration reduction of two sandwich beams connected by a joint with clearance, Mech. Syst. Sig. Process. 223 (2025) 111828.
[43] D. Upadrashta, Y. Yang, Nonlinear piezomagnetoelastic harvester array for broadband energy harvesting, J. Appl. Phys. 120 (5) (2016).
[44] W. Yang, S. Towfighian, A hybrid nonlinear vibration energy harvester, Mech. Syst. Sig. Process. 90 (2017) 317–333.
[45] W. Hayt, J. Buck, Eng. Electromagnet. (2012).
[46] L.I. Ye Kun, Modified kelvin pounding analytical model, Eng. Mech. A02 (2009) 245–248.
[47] D. Zhu, I. Duarte-Rabelo, I.N. Ayala-Garcia, A. Somov, An electromagnetic in-shoe energy harvester using wave springs, in: 2018 IEEE Industrial Cyber-Physical Systems (ICPS), IEEE, 2018, pp. 659–663.
[48] K. Fan, J. Liu, M. Cai, M. Zhang, T. Qiu, L. Tang, Exploiting ultralow-frequency energy via vibration-to-rotation conversion of a rope-spun rotor, Energ. Conver. Manage. 225 (2020) 113433.
[49] H.-X. Zou, Q.-W. Zhu, J.-Y. He, L.-C. Zhao, K.-X. Wei, W.-M. Zhang, R.-H. Du, S. Liu, Energy harvesting floor using sustained-release regulation mechanism for self-powered traffic management, Appl. Energy 353 (2024) 122082.
[50] Z. Yin, S. Gao, L. Jin, S. Guo, Q. Wu, Z. Li, A shoe-mounted frequency up-converted piezoelectric energy harvester, Sens. Actuat., A Phys. 318 (2021) 112530.
[51] K. Fan, H. Qu, Y. Wu, T. Wen, F. Wang, Design and development of a rotational energy harvester for ultralow frequency vibrations and irregular human motions, Renew. Energy 156 (2020) 1028–1039.
[52] M. Iqbal, F.U. Khan, M. Mehdi, Q. Cheok, E. Abas, M.M. Nauman, Power harvesting footwear based on piezo-electromagnetic hybrid generator for sustainable wearable microelectronics, J. King Saud University-Eng. Sci. 34 (5) (2022) 329–338.
[53] T. Jintanawan, G. Phanomchoeng, S. Suwankawin, P. Kreepoke, P. Chetchatree, C. U-viengchai, Design of kinetic-energy harvesting floors, Energies 13 (20) (2020) 5419.
[54] S. Liu, S. Liao, D. Liu, W. Qing, K. Wei, L. Zhao, H. Zou, A compact hybridized triboelectric-electromagnetic road energy harvester for vehicle speed measurement, DeCarbon (2024) 100036.